JOURNAL OF AIRCRAFT
Vol. 38, No. 2, March–April 2001

Vortical Flowfield Structure at Forward Swept-Wing Configurations

Christian Breitsamter* and Boris Laschka†
Technische Universität München, 85747 Garching, Germany

Extensive aerodynamic investigations have been carried out on forward swept-wing configurations with a wing sweep of −40 deg. A generic wing-body model with removable aft swept canards is used to measure the instantaneous velocities in several crossflow planes applying advanced hot-wire anemometry. The tests were made at 10-, 20-, and 30-deg angle of attack at a Reynolds number of 0.46×10^6. Detailed surveys of mean and rms velocities show that at moderate angles of attack strong wing leading-edge vortices are generated rotating opposite in a sense to the wing tip vortices. At higher incidences trailing-edge vortices are shed at the inner-wing part with the same sense of rotation as the wing tip vortices. The canard vortices pass the wing leading-edge relatively high, and after the onset of wing vortices they are moved upward and outboard. The interference between these vortices is studied in detail by analyzing the associated turbulent flow structure. Vortex bursting over the wing occurs already at moderate angles of attack. Downstream, the highest turbulence intensities are found in an annular region around the burst vortex core, where fluctuations are significantly channeled into a narrow band.

Nomenclature

C_D	=	drag coefficient, drag/$(q_\infty S_W)$
C_L	=	lift coefficient, lift/$(q_\infty S_W)$
C_m	=	pitching-moment coefficient, reference point N_{25}, nose-up positive, pitching moment/$(q_\infty S_W l_\mu)$
D_{core}	=	core diameter of burst wing leading-edge vortex, m
f	=	frequency, Hz
f_{dom}	=	dominant frequency, Hz
k	=	reduced frequency, $f l_\mu / U_\infty$
l_W	=	wing apex-tip distance, m
l_μ	=	wing mean aerodynamic chord, m
M	=	freestream Mach number
q_∞	=	freestream dynamic pressure, N/m^2
Re_{l_μ}	=	Reynolds number, $U_\infty l_\mu / \nu$
$S_{u'}$	=	spectral density of axial velocity fluctuations
S_W	=	wing area extended to $y_W = \tilde{y}_W = 0$ (Fig. 2), m^2
s	=	wing span, m
s_C	=	canard span, m
U_∞	=	freestream velocity, m/s
u, v, w	=	streamwise, lateral, and vertical velocity, m/s
$\bar{u}, \bar{v}, \bar{w}$	=	streamwise, lateral, and vertical mean velocity, m/s
u', v', w'	=	fluctuation part of u, v, w, m/s
$u_{\text{rms}}, v_{\text{rms}}, w_{\text{rms}}$	=	rms value of the fluctuating components of velocity, $u_{\text{rms}} = \sqrt{u'^2}$, $v_{\text{rms}} = \sqrt{v'^2}$, $w_{\text{rms}} = \sqrt{w'^2}$
$\bar{\boldsymbol{u}}_{yz}$	=	mean crossflow velocity vector
x, y, z	=	streamwise, lateral, and vertical coordinates of the wind-tunnel axis system, m
x_W, y_W, z_W	=	wing coordinates, origin at the tip, m
$\tilde{x}_W, \tilde{y}_W, \tilde{z}_W$	=	wing-fuselage coordinates, origin at the nose, m
Y, Z	=	local nondimensionalized coordinates of the measurement plane, referred to s, origin at the midsection
α	=	aircraft angle of attack, deg
ν	=	kinematic viscosity, m^2/s

Received 5 April 2000; revision received 10 October 2000; accepted for publication 11 October 2000.

*Dr.-Ing., Chief Scientist, Institute of Fluid Mechanics. Member AIAA.
†The Chair, Institute of Fluid Mechanics. Honorary Fellow AIAA.

Introduction

HIGH agility and poststall maneuvering are key factors in the design of future generation fighter aircraft.[1,2] Consequently, there is a need for high turn rates within a wide operational range as well as the capability to perform tactical maneuvers beyond maximum lift. In this context forward swept wing (FSW) configurations offer potential advantages.[3–5] FSWs are especially suited for canards, as the canard leading-edge vortices have a favourable influence on the flow of the inner wing area resulting in high usable lift.[6]

Concerning aerodynamic, structural, and aeroelastic properties, the main benefits of FSW can be summarized as follows: for an equal wing box sweep the FSW leading-edge sweep is smaller than that of the aft swept wing (ASW), whereas the FSW trailing-edge sweep is greater. Hence, the maximum leading-edge suction produced by the FSW is achieved at higher incidences. Induced drag will be correspondingly lower through which maximum lift over drag ratios are improved[7] (Fig. 1). However, this did not prove true for flight tests of the X-29A FSW aircraft as stated below.

On ASWs maximum lift is limited by tip stall at a lift coefficient for which the large inner wing area is far from its limiting lift. For negative wing sweep the aerodynamic lifting potential of the inner wing is exploited to an ever increasing degree. Because of this, the FSW can be expected to produce a higher maximum lift coefficient than the ASW. An untwisted aeroelastically tailored FSW can exhibit an almost ideal lift distribution at all subsonic points of the flight envelope.[8] At high subsonic Mach numbers the FSW will sustain a higher preshock Mach number and hence a larger lift coefficient for the same pressure jump across the shock. For the high-speed flight regime there are no significant profits.

In general, on ASWs boundary-layer separation begins in the tip region, whereas on FSWs the root area stalls first. Because of the smaller roll and yaw disturbances and the undiminished roll control power, flow separation effects such as wing drop, wing rock, and nose slice may be considerably less severe on FSWs. Therefore, FSW configurations are stable in yaw and roll up to high angles of attack. Moreover, the relocation of wing lift from the tip region to the root area provides the FSW with high aileron effectiveness even beyond maximum lift. Thus, there are appreciable advantages at subsonic speeds, in particular, for the high-angle-of-attack performance. For weight reduction the lower tip aerodynamic loading

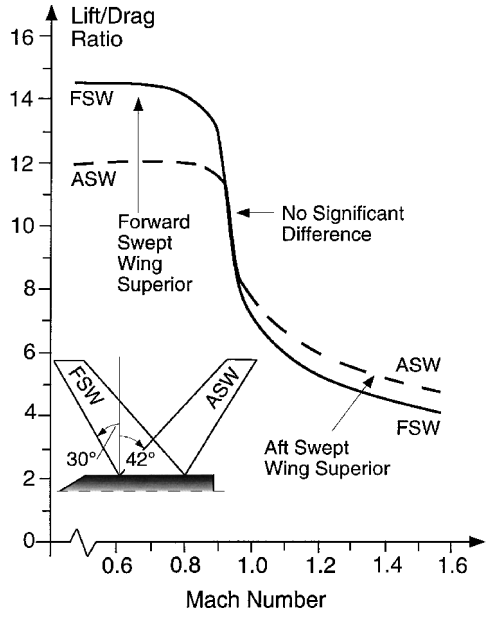

Fig. 1 Comparison of the maximum lift-to-drag ratios of generic FSW and ASW (of the same area and aspect ratio).[7]

of FSWs allows the use of a higher wing taper on the FSW than is possible for the ASW.[9]

The main aeroelastic disadvantage of the FSW is the reduction in divergence speed as sweep is reduced from aft to forward. It has been a main reason for not exploiting the aerodynamic benefits of FSWs in high-performance fighter aircraft. The introduction of carbon-fiber composites in aircraft structures has eliminated this obstacle. The FSW main aeroelastic advantages are its aileron efficiency and the very high aileron reversal speed. For the same reason active control technology, using outboard flaps, could be applied more efficiently on FSWs.

Extensive investigations on the FSW aerodynamic characteristics were performed in the decade from 1975 to 1985 to develop the FSW concept for flight demonstration.[5,7–11] The efforts result in the X-29A FSW Advanced Technology Demonstrator program[12] integrating key technologies like close-coupled variable incidence canards, supercritical thin airfoil, variable camber, aeroelastic tailoring, and composite primary structure. Contrary to generic model tests (Fig. 1), in-flight measurements of the X-29A FSW aircraft at subcritical speed ($M = 0.6$) and incidences up to $\alpha = 16$ deg ($C_L \approx 1.6$) show no significant improvements on lift-to-drag ratios in comparison to contemporary high-performance ASW aircraft.[13] Further, at critical speed ($M = 0.9$) the X-29A aircraft performance was probably penalized by underwing actuators and hinges. However, for FSW configurations only few flowfield studies were reported. Griffin[14] and Griffin et al.[15,16] presented distributions of steady crossflow velocities and total pressure coefficients. Unsteady flowfields were not measured.

As a contribution to fill this gap, a research program on generic FSW configurations was initiated at the Lehrstuhl für Fluidmechanik of the Technische Universität München.[17] These investigations are aimed at providing detailed insight into the flow physics of FSW configurations. Systematic aerodynamic tests have been conducted, which focus on the flow phenomena at moderate and high angles of attack. In particular, the complex vortex systems are studied comparing the separation topology with the known features of delta and of aft swept wings. The results obtained contribute to the knowledge on leading-edge vortex flows, which is essential for future fighter aircraft design. The turbulent flow structure is also carefully investigated. The related database is needed to quantify the excitation input associated with aeroelastic phenomena like buffeting on wing or fin(s). Moreover, the comprehensive flowfield surveys are of distinct utility for the development and validation of computational fluid dynamics methods.

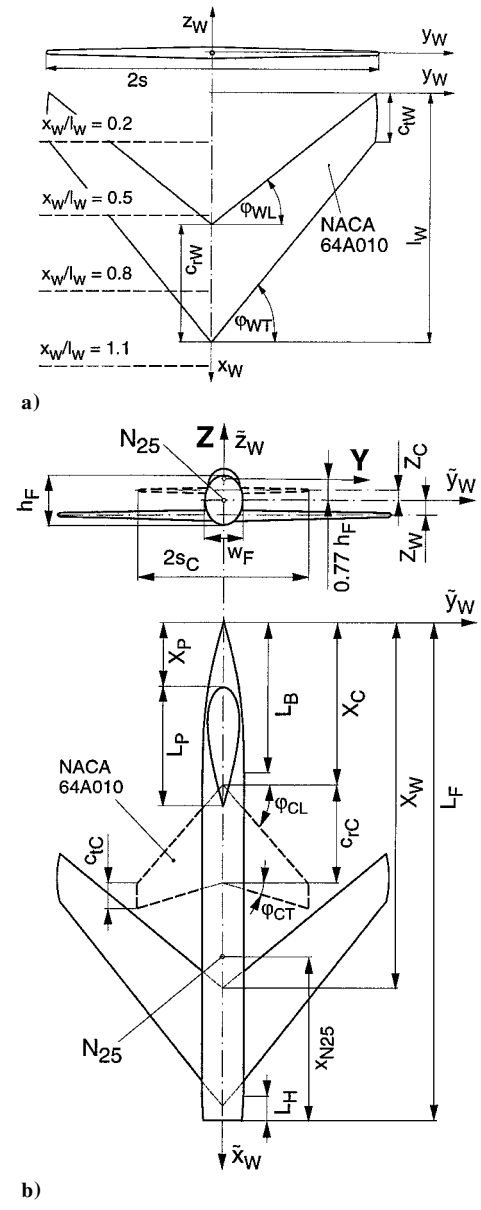

Fig. 2 Geometry of wind-tunnel models of a) wing and b) wing-body/wing-body-canard configuration.

Measurement Technique and Test Program

Description of Models and Facility

The experiments were performed on a single 40-deg forward swept wing[17] as well as on a generic wing-body configuration fitted with the identical wing planform (Fig. 2). The modular conception of the wing-body model enables the mounting of canards and/or strakes. The geometric data of the configurations tested are collected in Table 1. This paper presents results of the investigations on the wing-body model with and without an aft swept canard. The airfoil of the wing and canard is the NACA 64A010. The fuselage of the wing-body model is formed as an elliptic cylinder with a canopy. The nose section is inclined downward at an angle of 5 deg. All model parts are made of carbon-fiber composites with steel inlets.

The experiments were carried out in a Göttingen type low-speed wind-tunnel facility of the Lehrstuhl für Fluidmechanik of the Technische Universität München. The open test section is of circular shape with 1.5 m diam and 3 m length. Maximum usable velocity is 55 m/s. Turbulence intensity ranges from 0.3–0.4%. The test section is equipped with a three-axis model support and a three-degree-of-freedom probe-traversing system. The models were sting mounted on their lower surfaces from the moving support strut (Fig. 3), ensuring that flowfield measurements are to a great extent free from

Table 1 Geometric data of FSW configurations

Geometric quantities	Symbols and values
Wing	
Leading-edge sweep	$\varphi_{WL} = -40.0$ deg
Trailing-edge sweep	$\varphi_{WT} = -52.2$ deg
Aspect ratio	$A_W = 3.81$
Taper ratio	$c_{tW}/c_{rW} = 0.40$
Span	$2s = 0.60$ m
Mean aerodynamic chord	$l_\mu = 0.167$ m
Geometric neutral point N_{25}	$x_{N25}/l_W = 0.354$
Canard	
Leading-edge sweep	$\varphi_{CL} = 49.0$ deg
Trailing-edge sweep	$\varphi_{CT} = 25.5$ deg
Aspect ratio	$A_C = 3.14$
Taper ratio	$c_{tC}/c_{rC} = 0.30$
Relative span	$s_C/s = 0.54$
Fuselage	
Length/height ratio	$L_F/h_F = 10$
Height/width ratio	$h_F/w_F = 1.19$
Front part length	$L_B/h_F = 2.63$
Rear part length	$L_H/h_F = 0.53$
Canopy length	$L_P/h_F = 2.37$
Position of canopy	$X_p/L_F = 0.13$
Combination Wing-Fuselage	
Relative fuselage length	$L_F/2s = 1.58$
Relative fuselage width	$w_F/2s = 0.13$
Relative wing position	$X_W/L_F = 0.74$, $Z_W/h_F = 0.32$
Combination Canard-Fuselage	
Relative canard position	$X_C/L_F = 0.32$, $Z_C/h_F = 0.21$

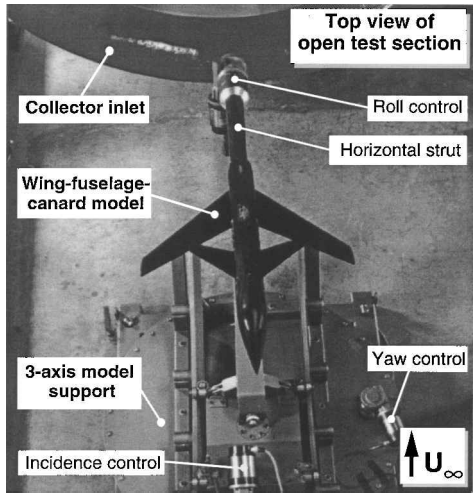

Fig. 3 Wing-body-canard model mounted in the test section (top view).

interference. The computer-controlled model support strut provides an incidence range from 0 to 31.5 deg, and the models may be yawed and rolled 360 deg. Probes can be traversed in the streamwise, spanwise, and normal directions with minimum steps of ±0.1 mm.

Measurement of Instantaneous Velocity

To measure the fluctuating velocities, dual-sensor hot-wire probes were used. The sensors consist of 5-μm-diam platinum-plated tungsten wires giving a length/diameter ratio of 250. The measuring volume formed by the wires is approximately 0.8 mm in diameter and 0.5 mm in height. A sensor angle of 45 deg is chosen assuming that the best angular resolution will be obtained with pairs of perpendicular wires. An additional temperature probe is employed to correct the anemometer output voltages if ambient flow temperature varies.

The probes were operated by a multichannel constant-temperature anemometer system. By means of its signal conditioner modules, bridge output voltages were low-pass filtered at 1000 Hz before digitization and amplified for optimal signal level. The signals were then digitized with 12-bit precision through the 16-channel

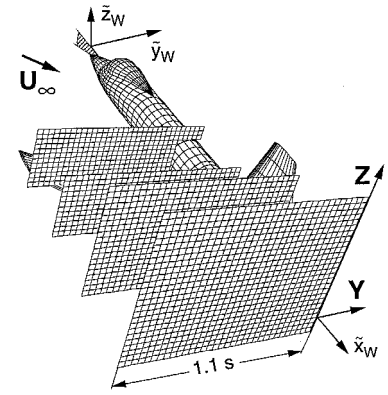

Fig. 4 Size and grid resolution of measurement planes used for wing-body tests at α = 20 deg (for coordinate systems see Fig. 2).

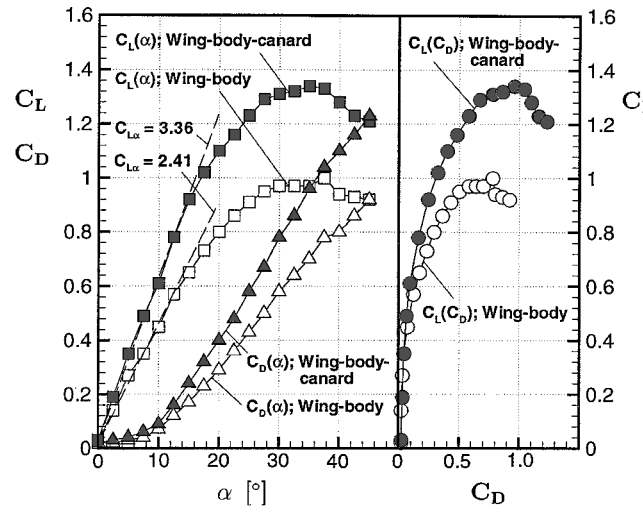

a) Lift and drag coefficient

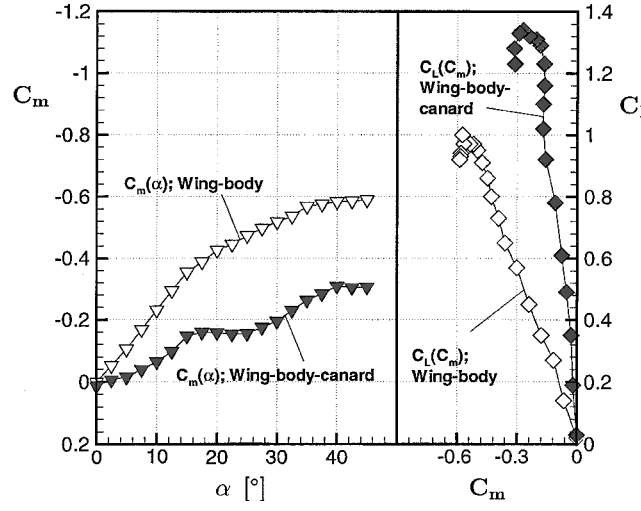

b) Pitching-moment coefficient

Fig. 5 Results of force and moment measurements for the canard-off and the canard-on configuration at $Re_{l_\mu} = 0.46 \times 10^6$.

simultaneous-sampling A/D converter of the PC high-speed board. The sampling rate for each channel was set to 3000 Hz giving a Nyquist frequency of 1500 Hz. The sampling time was 26.24 s so that each sample block contains 78,720 points. These parameters were achieved by preliminary tests to ensure that all significant flowfield phenomena were detected. Statistical accuracy of the calculated quantities was considered as well. Random error calculations gave accuracies of 0.2, 1, and 3% for the mean and standard deviation and spectral density estimation, respectively.[18]

The use of a cross-wire configuration generally assumes some knowledge of the flowfield, such as a known flow direction to which the probe must be aligned. The nature of the vortex-dominated flow precludes any knowledge on the direction of the velocity vector everywhere in the field, save for the axial component, which is assumed to be always in the positive x direction. To determine the three velocity components (u, v, w), the probe has to be rotated around its axis by 90 deg to adjust the wire plane once horizontal and once vertical against the main flow direction. Thus, two triggered traverse sweeps were necessary to obtain the streamwise u, lateral v, and vertical w components, respectively. Each digitized and temperature corrected voltage pair of the corresponding probe positions was converted to evaluate the time-dependent velocity vector. The numerical method used is based on look-up tables derived from the full velocity and flow angle calibration of the sensors. A detailed description is given in Refs. 19 and 20.

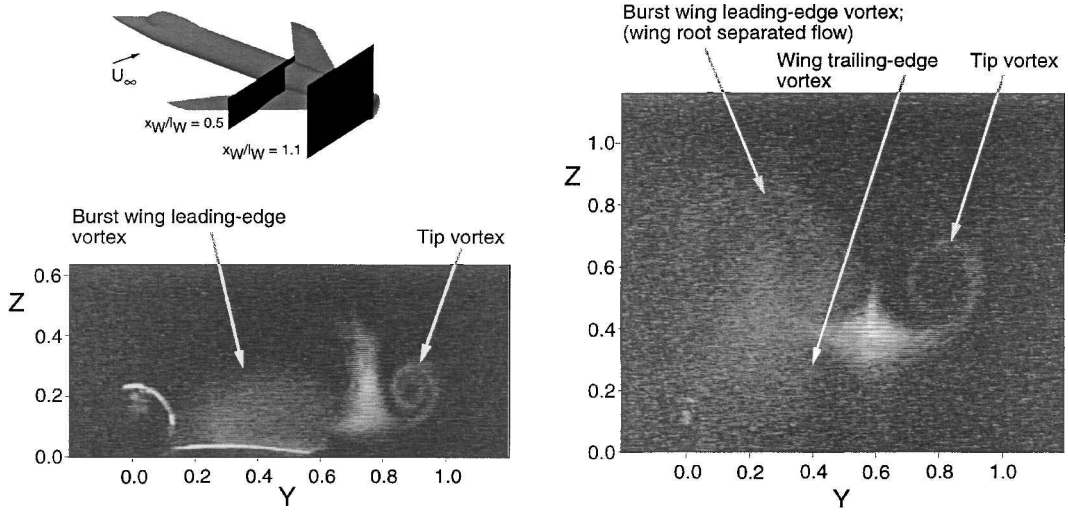

a) $x_W/l_W = 0.5$ b) $x_W/l_W = 1.1$

Fig. 6 Laser light sheet flow visualization for the wing-body configuration at measurement stations. x_W/l_W = 0.5, and 1.1 for α = 30 deg and $Re_{l_\mu} = 0.17 \times 10^6$ (view from front).

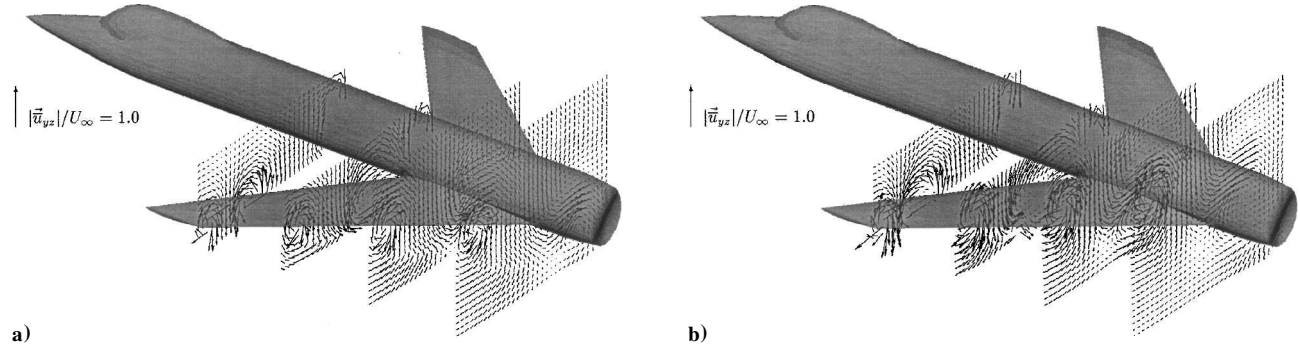

a) b)

Fig. 7 Wing-body crossflow velocity vectors $\vec{u}_{yz}$ at measurement stations x_W/l_W = 0.2, 0.5, 0.8, and 1.1 for a) α = 20 and b) 30 deg and $Re_{l_\mu} = 0.46 \times 10^6$.

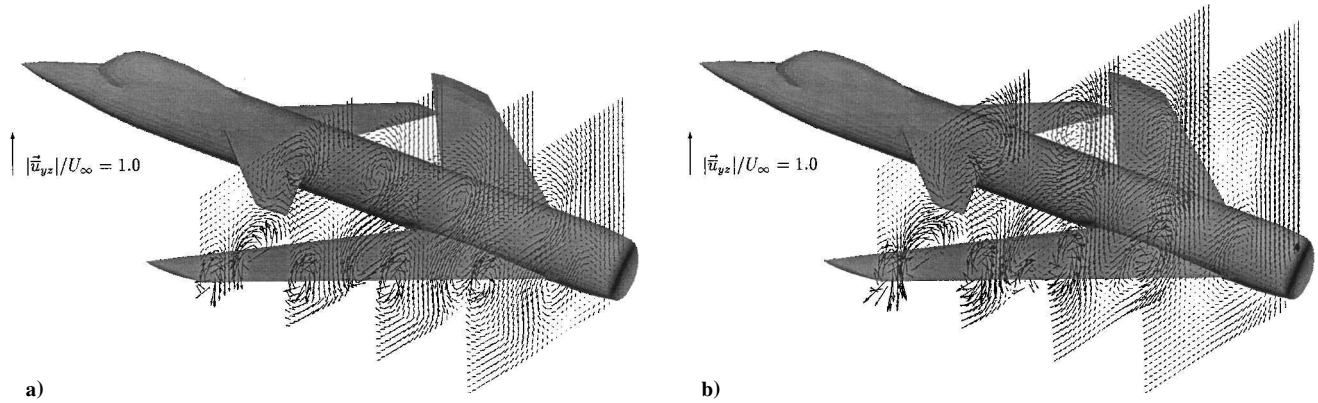

a) b)

Fig. 8 Wing-body-canard crossflow velocity vectors $\vec{u}_{yz}$ at measurement stations x_W/l_W = 0.2, 0.5, 0.8, and 1.1 for a) α = 20 and b) 30 deg and Re_{l_μ} = 0.46×10^6.

Description of Tests

The overall aerodynamic behaviour was documented by six-component measurements using a strain-gauge strut balance. The angle of attack range $0 \leq \alpha \leq 45$ deg was covered with steps of $\Delta\alpha = 2.5$ deg at constant reference velocity U_∞ of 40 m/s. This corresponds to a Reynolds number of $Re_{l_\mu} = 0.46 \times 10^6$ based on the wing mean aerodynamic chord. Local atmospheric conditions prescribed the test section static pressure and temperature. Within these experiments transition was not fixed. Evaluating the force and moment measurements, open test section corrections were applied to the data, and angles of attack were also corrected.

Flowfield measurements were conducted in four planes perpendicular to the model x_W axis. Three planes were located over the port wing at stations $x_W/l_W = 0.2$, 0.5, and 0.8, and one in the wake at $x_W/l_W = 1.1$ (Fig. 2). The tests were carried out at angles of attack of 10, 20, and 30 deg at symmetric freestream at the test Reynolds number of $Re_{l_\mu} = 0.46 \times 10^6$. For all measurement planes the lateral distance was 1.1 s, thus covering all relevant flowfield phenomena. The vertical extension was adapted to the expansion of the vortex systems known from laser light sheet tests. The survey points were evenly spaced, giving a relative grid resolution of 0.016 in both the spanwise and vertical direction based on the wing span. This is illustrated by Fig. 4, depicting size and grid resolution of the measurement planes for the wing-body tests at $\alpha = 20$ deg.

Regarding the susceptibility of vortex flow structures to intrusive measurements, particularly at the breakdown process, probe interference is minimized by using miniature hot-wire probes connected to long, thin, and stiff probe holders (2.5 mm in diameter). The probe holder itself is mounted on the traverse system vertical sting (5.5 mm in diameter) moved in a minimum blockage arrangement. In this context the accuracy of probe measurements on leading-edge vortex flows was investigated, for example, by Payne[21]

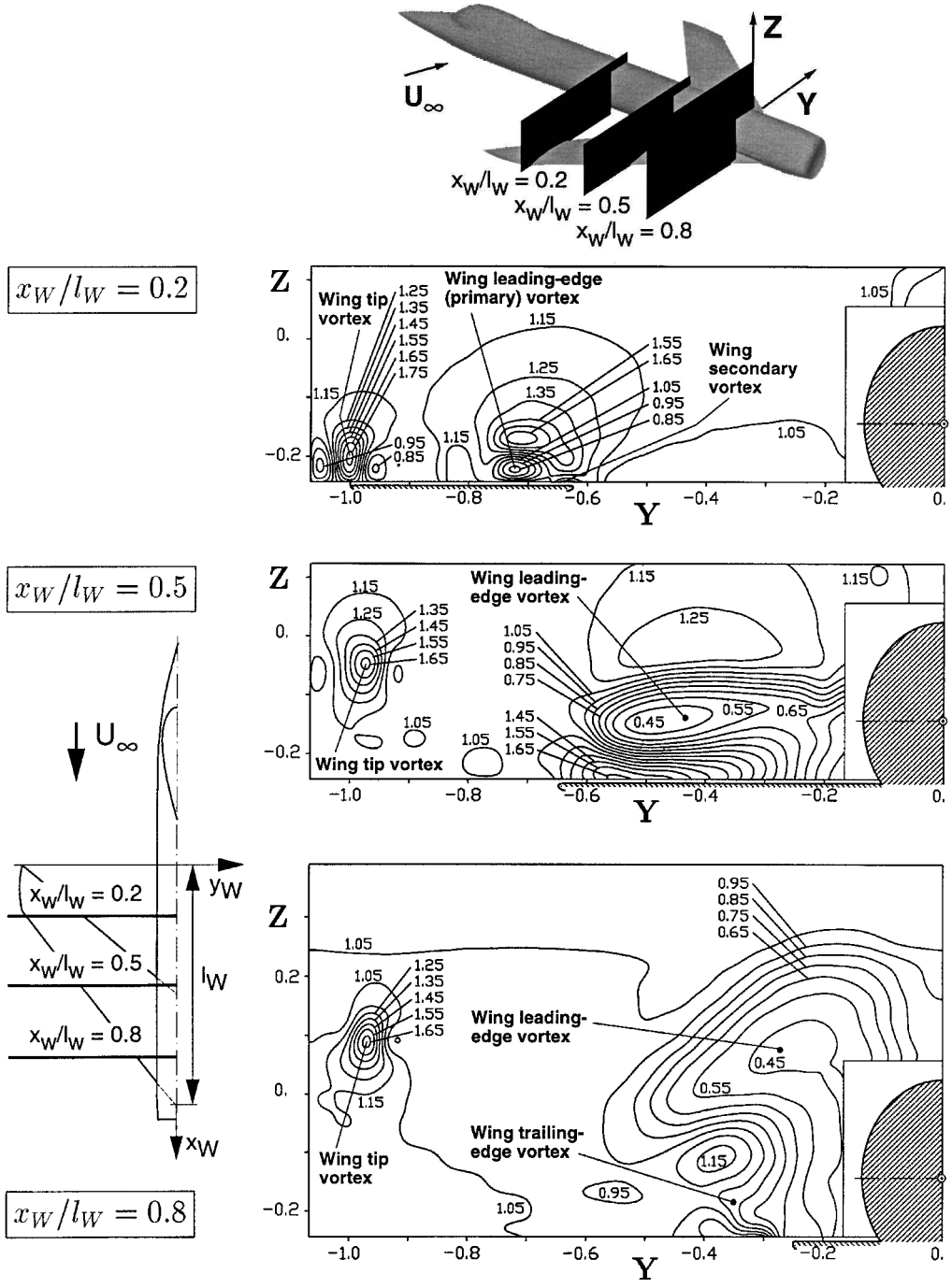

Fig. 9 Contours of mean axial velocity $\bar{u}/U_\infty$ over the wing-body configuration at $\alpha = 20$ deg and $Re_{l_\mu} = 0.46 \times 10^6$. Chordwise measurement stations x_W/l_W = a) 0.2, b) 0.5, and c) 0.8.

and Payne et al.,[22] comparing laser Doppler velocimeter measurements with and without a seven-hole probe in place. Beside the size of the probe, the influence on vortex breakdown depends on the probe position relative to the breakdown location and also on the natural breakdown location over the wing. The most sensitive case refers to vortex breakdown near the wing trailing edge where the adverse pressure gradient reaches its maximum. There, the placing of a probe may shift the breakdown location markedly upstream. However, probe disturbances are of minor relevance if vortex breakdown takes place well upstream of the trailing edge as it is the case for the flowfields presented herein. Especially for the measurement plane at $x_W/l_W = 0.2$, where the distance of probe position to breakdown location becomes a minimum for the considered incidences, probe interference was studied using laser light sheet tests and liquid crystal surface flow visualization with and without the probe in place. No significant effects of the probe and its support system on vortex breakdown locations and vortical flow structures were detected.

Results and Discussion

Force and Moment Coefficients

Results of the six-component measurements, namely lift, drag, and pitching-moment curves are shown in Fig. 5 for both the wing-body and wing-body-canard configuration. Already for low angles

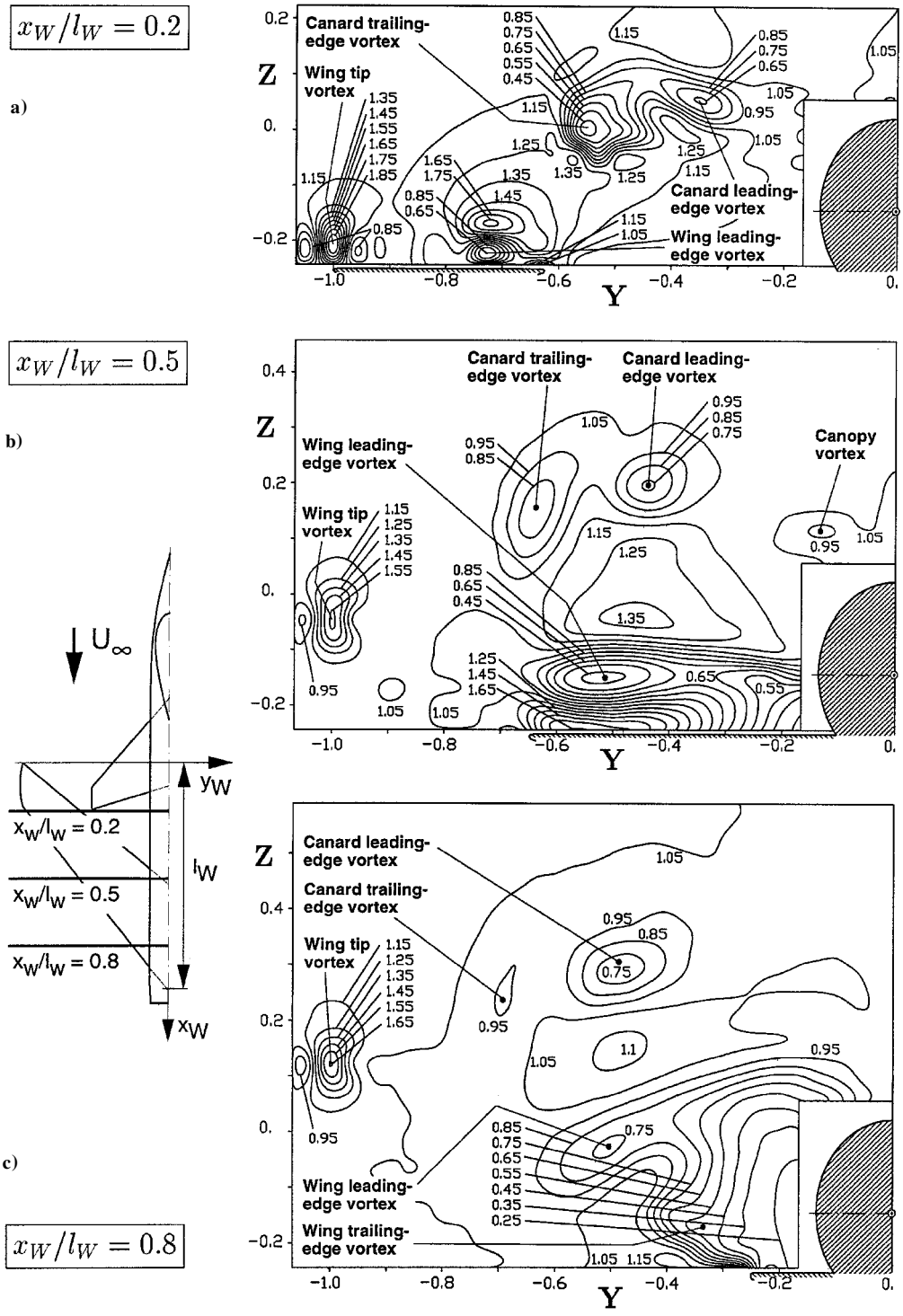

Fig. 10 Contours of mean axial velocity $\bar{u}/U_\infty$ over the wing-body-canard configuration at $\alpha = 20$ deg and $Re_{l_\mu} = 0.46 \times 10^6$. Chordwise measurement stations x_W/l_W = a) 0.2, b) 0.5, and c) 0.8.

of attack ($\alpha \leq 10$ deg) the lift and pitching-moment coefficients of the two configurations differ significantly, whereas differences in the drag coefficients are only small. In comparison to canard-off, the canard-on configuration is characterized by a substantial higher lift gradient and higher lift maximum (Fig. 5a). The corresponding increase in induced drag at higher angles of attack contributes mainly to the larger total drag of the canard-on configuration for $\alpha > 10$ deg. The lift-drag polars exhibit symmetric distributions. Further, the pitching-moment curves indicate that with respect to the moment reference point the addition of the canards decreases significantly the nose-down pitching moment (Fig. 5b). In particular, at $\alpha \approx 8 \div 10$ deg the influence of the fully developed wing leading-edge vortices on the aerodynamic characteristics is documented by additional lift and, therefore, a larger nose-up pitching moment. These effects are reflected by slight nonlinearities in the slope of the lift and pitching-moment curves for both configurations. Bursting of the wing leading-edge vortices over the wing at midroot chord takes place for canard-off at $\alpha \approx 11.5$ deg and for canard-on at $\alpha \approx 13$ deg leading to a subsequent drop in the functions of lift and pitching-moment coefficients vs angle of attack. Because of leading-edge vortex flow, the region of maximum lift obtained for canard-off is relatively flat covering an incidence range of approximately $30 \div 38$ deg, whereas for canard-on the corresponding plateau becomes smaller.

Flow Visualization

Laser light sheet tests were made to determine the evolution of the vortex systems, mainly produced by the FSW and for the canard-on configuration by the aft swept canard. Results shown here depict light sheets at $x_W/l_W = 0.5$ and 1.1 obtained for canard-off

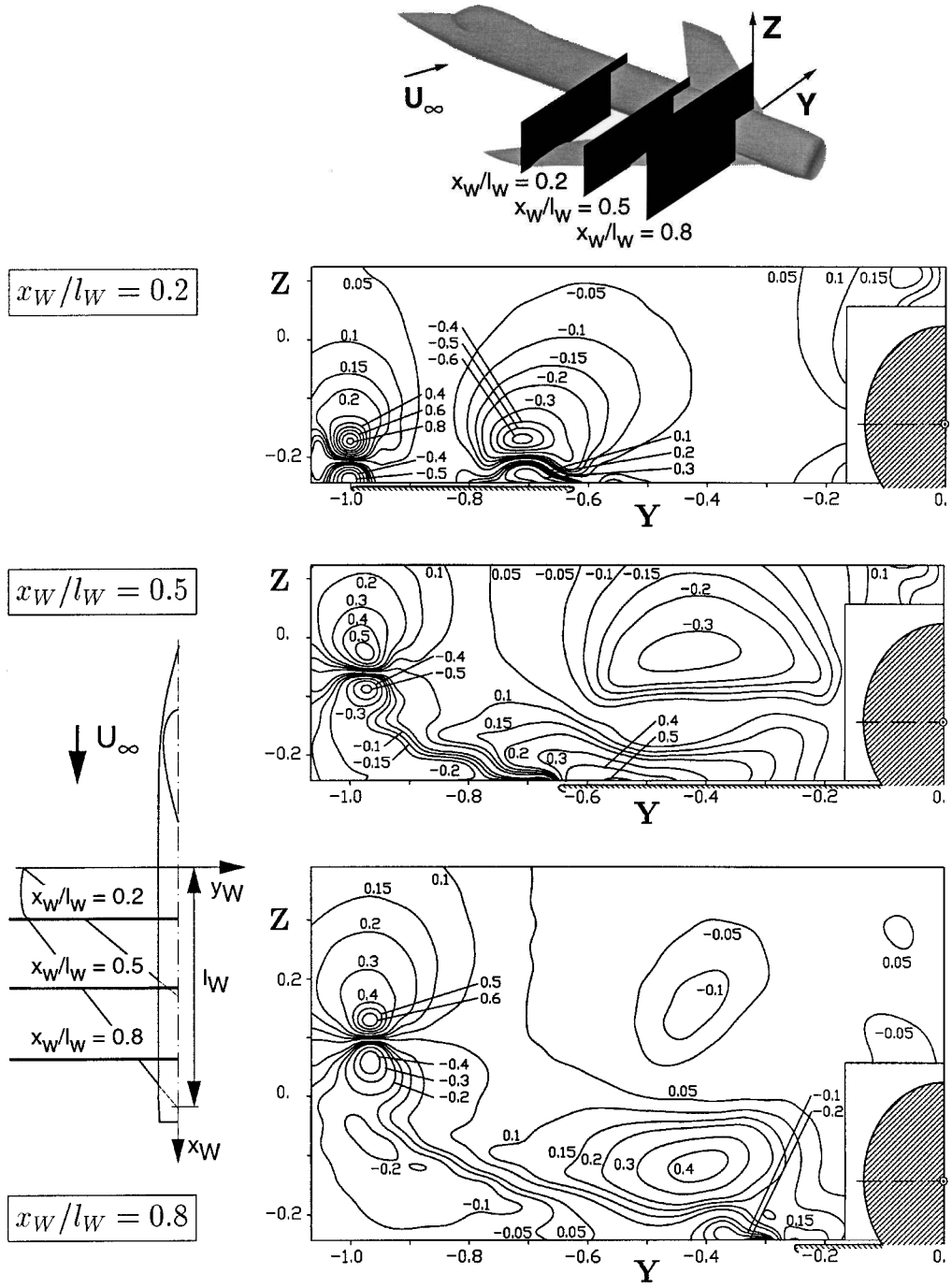

Fig. 11 Contours of mean lateral velocity $\bar{v}/U_\infty$ over the wing-body configuration at α = 20 deg and $Re_{l_\mu} = 0.46 \times 10^6$. Chordwise measurement stations x_W/l_W = a) 0.2, b) 0.5, and c) 0.8.

at $Re_{l_\mu} = 0.17 \times 10^6$ and $\alpha = 30$ deg (Fig. 6). At $x_W/l_W = 0.5$ the cross section of the FSW leading-edge vortex is of elliptical shape and has strongly expanded indicating that bursting occurs far upstream. The tip vortex is well defined by the corresponding rolled-up shear layers. Downstream at $x_W/l_W = 1.1$, the FSW leading-edge vortex becomes further enlarged resulting in a big region of highly fluctuating flow. The tip vortex grows also in size. An additional vortical structure can be identified behind the inner wing part representing the wing trailing-edge vortex. Based on the laser light sheet tests, survey locations and extensions of the time-consuming probe measurements were defined.

Mean Velocity Surveys

The three-dimensional flowfield over the port wing is documented both by crossflow velocity vectors (Figs. 7 and 8) and by contours of streamwise and lateral velocities (Figs. 9–12). The flowfields of the wing-body and wing-body-canard configuration are characterized by the interaction of several vortex systems. At $\alpha = 20$ deg the FSW tip and leading-edge vortex as well as the canard leading- and trailing-edge vortex are clearly visible by the induced crossflow velocities (Figs. 7a and 8a). Contrary to delta or aft swept wings, the tip and leading-edge (primary) vortex of the FSW are counter-rotating. For both the canard-on and canard-off configuration the

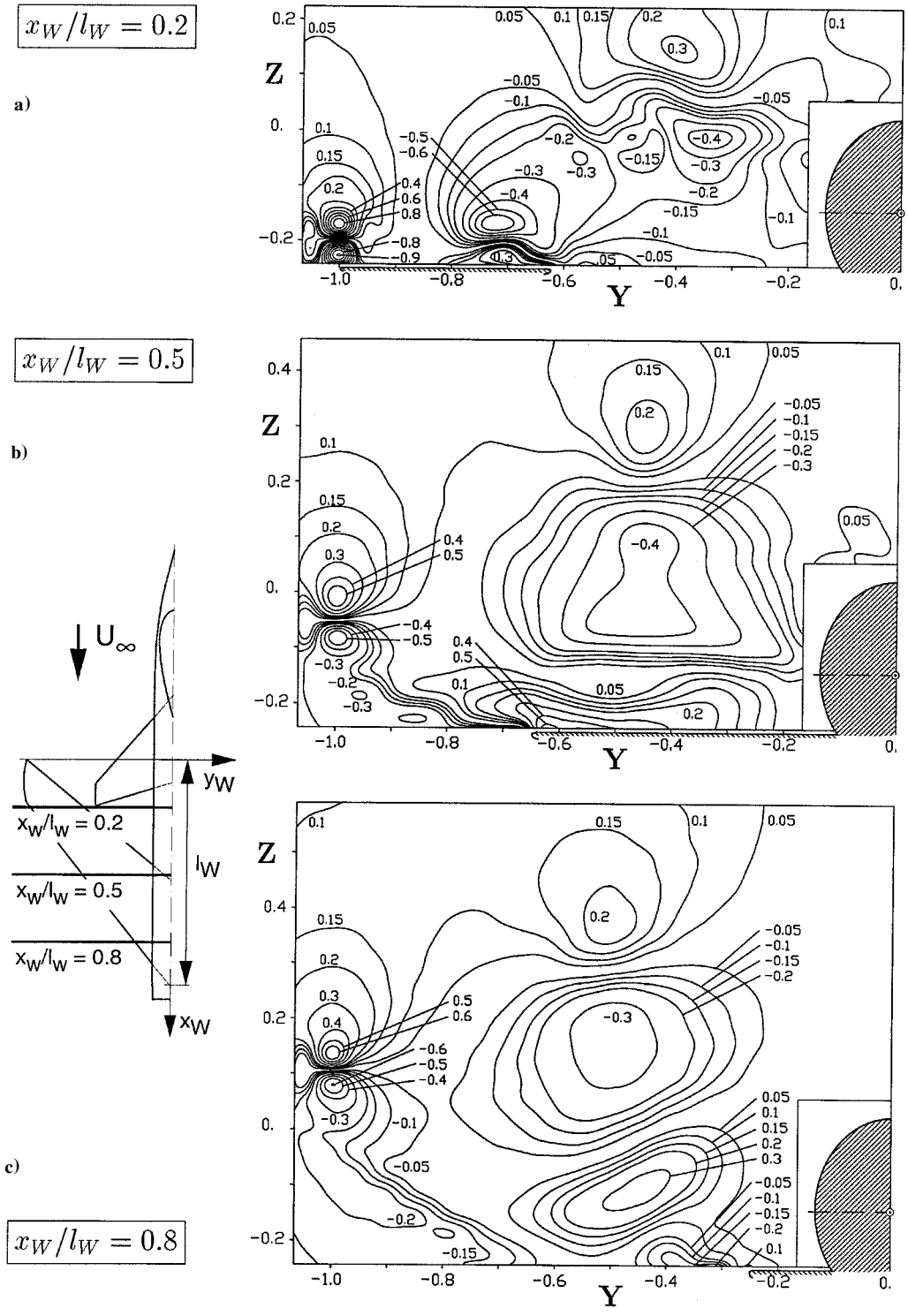

Fig. 12 Contours of mean lateral velocity $\bar{v}/U_\infty$ over the wing-body-canard configuration at $\alpha = 20$ deg and $Re_{l_\mu} = 0.46 \times 10^6$. Chordwise measurement stations x_W/l_W = a) 0.2, b) 0.5, and c) 0.8.

cross section of the wing leading-edge vortex is formed elliptically even in the most upstream plane and a region of reduced velocity dominates the vortex core flow. This indicates that the wing leading-edge vortex is already in a postbreakdown stage. From oil-flow patterns the burst position is determined at $x_W/l_W = 0.11$ for the wing-body and at $x_W/l_W = 0.16$ for the wing-body-canard configuration, respectively.[23] With increasing incidence $\alpha = 30$ deg, the vortex systems are strongly enlarged producing higher crossflow components than at $\alpha = 20$ deg (Figs. 7b and 8b). Bursting of the wing leading-edge vortex takes place close to the wing tip, particularly, at $x_W/l_W = 0.05$ for the wing-body and at $x_W/l_W = 0.09$ for the wing-body-canard configuration.[23] Thus, the wing leading-edge vortex shows a big core region of very low velocity. The canard leading-edge vortex is bursted at $\alpha = 20$ and 30 deg as well. However, over the wing a more concentrated canard vortex system can be observed.

At $\alpha = 20$ deg and $x_W/l_W = 0.2$ the wing-body mean velocity distribution indicates the center of the wing tip vortex by the peak axial velocity ($\bar{u}/U_\infty = 1.75$) at $Y = -1.01$, $Z = -0.20$ (Fig. 9a). For better identification the different vortex centers are marked in the figures. For the burst wing leading-edge vortex the center is detected by a minimum of axial velocity ($\bar{u}/U_\infty = 0.85$) at $Y = -0.72$, $Z = -0.22$. A secondary vortex is located at $Y = -0.64$, $Z = -0.24$ (Figs. 9a and 11a). The secondary vortex is rather small because the boundary layer on the wing beneath the leading-edge vortex is turbulent. At $x_W/l_W = 0.5$ the core of the burst wing leading-edge vortex increases strongly in its radial extension. It shows an axial velocity deficit with $\bar{u}/U_\infty = 0.45$ (Fig. 9b). Above and below the core region the axial flow is accelerated reaching a maximum of $\bar{u}/U_\infty = 1.65$ close to the wing surface. The induced lateral velocity is 30% of U_∞ above the core and 50% of U_∞ near the wing surface (Fig. 11b). There, the deflection of the flow is inward, whereas on an ASW this deflection is outward. Downstream at $x_W/l_W = 0.8$, the leading-edge vortex moves further inboard and upward (Fig. 9c). Thus, above the fuselage the port wing vortex sheets come in contact with the starboard ones. Although the vortex core becomes very large, a well-structured swirling flow pattern can be observed around it. At $Y = -0.38$, $Z = -0.19$, a trailing-edge vortex is found with a rotation opposite to the one of the leading-edge vortex (Fig. 11c). More downstream, the trailing-edge vortex is embedded in the shear layer of the dominant leading-edge vortex. In the wake ($x_W/l_W = 1.1$) the wing primary vortex starts to dissipate, but it is strong enough to move the trailing-edge vortex inboard and upward.[17]

For the wing-body-canard configuration the overall vortex structure is significantly changed (Figs. 10 and 12). At $x_W/l_W = 0.2$ the axial velocity contours denote that the canard vortex system consists of a burst leading-edge vortex ($Y = -0.35$, $Z = 0.06$) and a tip vortex combined with a trailing-edge vortex ($Y = -0.55$, $Z = 0.01$) (Figs. 10a and 12a). Because of the canard influence, the wing leading-edge vortex produces higher axial and lateral velocities compared to the canard-off configuration. Moreover, the inner portion of the wing encounters the accelerated flow evoked by the canard through which the wing leading-edge vortex is embedded in a higher suction level than for the noninterfering case. Therefore, the burst position of the wing leading-edge vortex is shifted downstream in comparison to canard-off. At $x_W/l_W = 0.5$ the canard vortex system pushes the wing leading-edge vortex downward to the wing surface (Figs. 10b and 12b). The wing leading-edge vortex strength is again higher than for canard-off. At $x_W/l_W = 0.8$, compared to the wing-body case, the wing leading-edge vortex is also moved closer to the wing surface, whereas the induced crossflow velocities are not markedly increased (Figs. 10c and 12c).

The presentation of these results reveals that there is a strong influence of the canard on the wing. The canard produces behind its trailing edge a downwash field within its span and an upwash field outside its span. The upwash field increases the effective angle of attack in the forward and outside portion of the wing, which supports

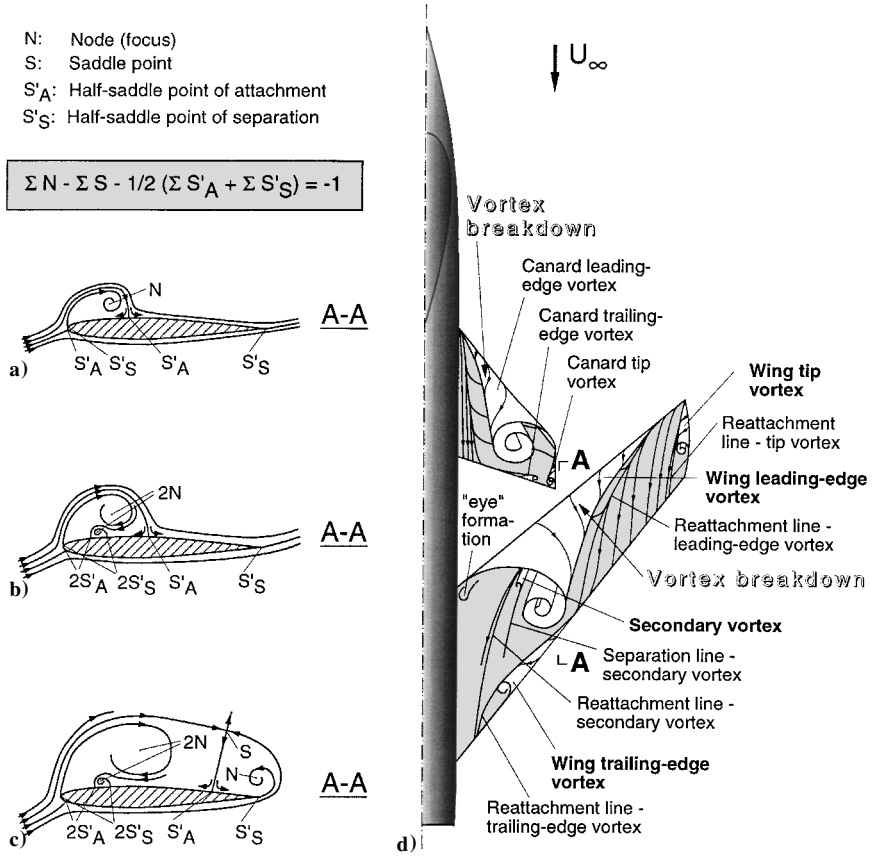

Fig. 13 Schematic representation of the vortex flow features over the wing-body-canard configuration at moderate and high angles of attack. Flow topology of a spanwise wing section A-A for a) $\alpha \approx 10$ deg, b) $\alpha \approx 20$ deg, and c) $\alpha \approx 30$ deg. Three-dimensional vortical flow sketch for d) $\alpha \approx 20$–30 deg.

flow separation there. The downwash field reduces the effective angle of attack in the innner and rear portion of the wing. This leads to a suppression of flow separation there, which is especially favorable for delaying stall at the wing root area. Because of the nonuniform distribution of the effective angle of attack along the wing leading edge, the wing primary vortex is fed with vorticity in a different manner than for the canard-off configuration. For this reason the wing vortices evoke higher crossflow velocities in the outer wing part than for the noninterfering case. The influence of the wing leading-edge vortex on the canard vortices is such that the canard vortex system is moved outboard and upward. The wing induced-flow acceleration reinforces the canard vortex system over the wing, through which it still keeps its structure downstream behind the wing trailing edge.

The development of the mean flowfield is summarized in Fig. 13 depicting the flow topology of an inner wing section from moderate to high angles of attack supplemented by a schematic three-dimensional representation. The topology rule used can be taken from Ref. 24. For moderate angles of attack, a leading-edge vortex develops, which is placed close to the wing surface (Fig. 13a). Bursting occurs already in the outer wing part. The vortex-induced pressure gradients are too small to cause a secondary separation. At

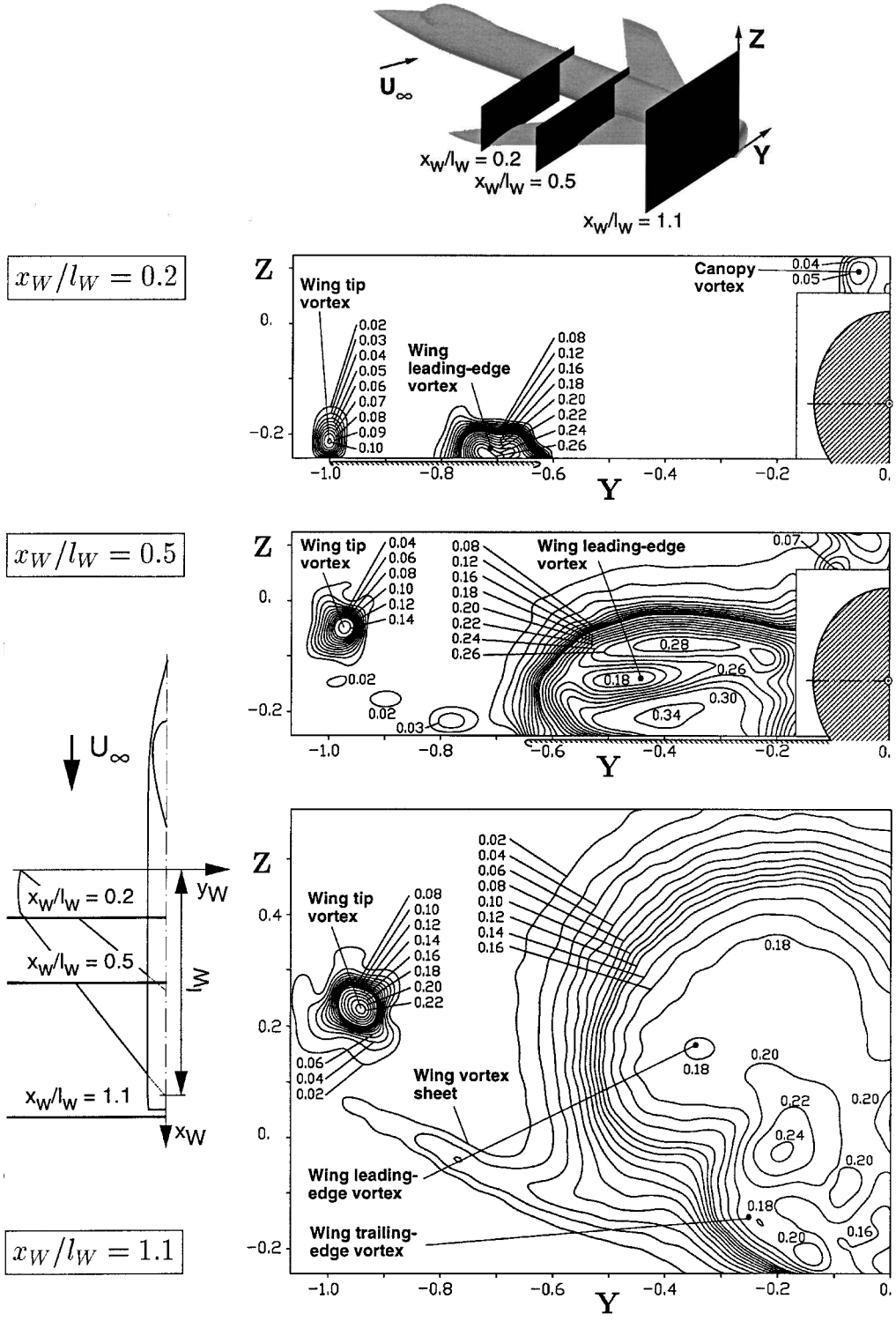

Fig. 14 Contours of axial rms velocity u_{rms}/U_∞ over the wing-body configuration at α = 20 deg and $Re_{l_\mu} = 0.46 \times 10^6$. Chordwise measurement stations x_W/l_W = a) 0.2, b) 0.5, and c) 1.1.

higher incidences the wing leading-edge vortex grows both in size and strength so that a secondary vortex is formed (Fig. 13b). With further increasing incidence the trailing-edge vortex sheet emanating from the inner wing rolls up into a trailing-edge vortex, the rotation of which is opposite to the leading-edge vortex (Fig. 13c). The axis of the leading-edge vortex initially points inboard on the wing, before being aligned with the freestream direction. Because of fuselage blockage, an eye-like shaped dead flow region develops at the forward wing root area formed by an upstream and outboard bending of the separation line associated originally to the wing leading-edge vortex. At canard-off the wing root area is then characterized by a disorganized, separated flow.[17] At high α the canard vortex system consists also of a leading-edge vortex, a small trailing-edge vortex, and a tip (side-edge) vortex (Fig. 13d). At canard-on the strength of the wing leading-edge vortex is increased in the outside portion of the wing. Moreover, the wing leading-edge vortex is placed closer to the wing surface suppressing also the large dead flow region at the wing root area.

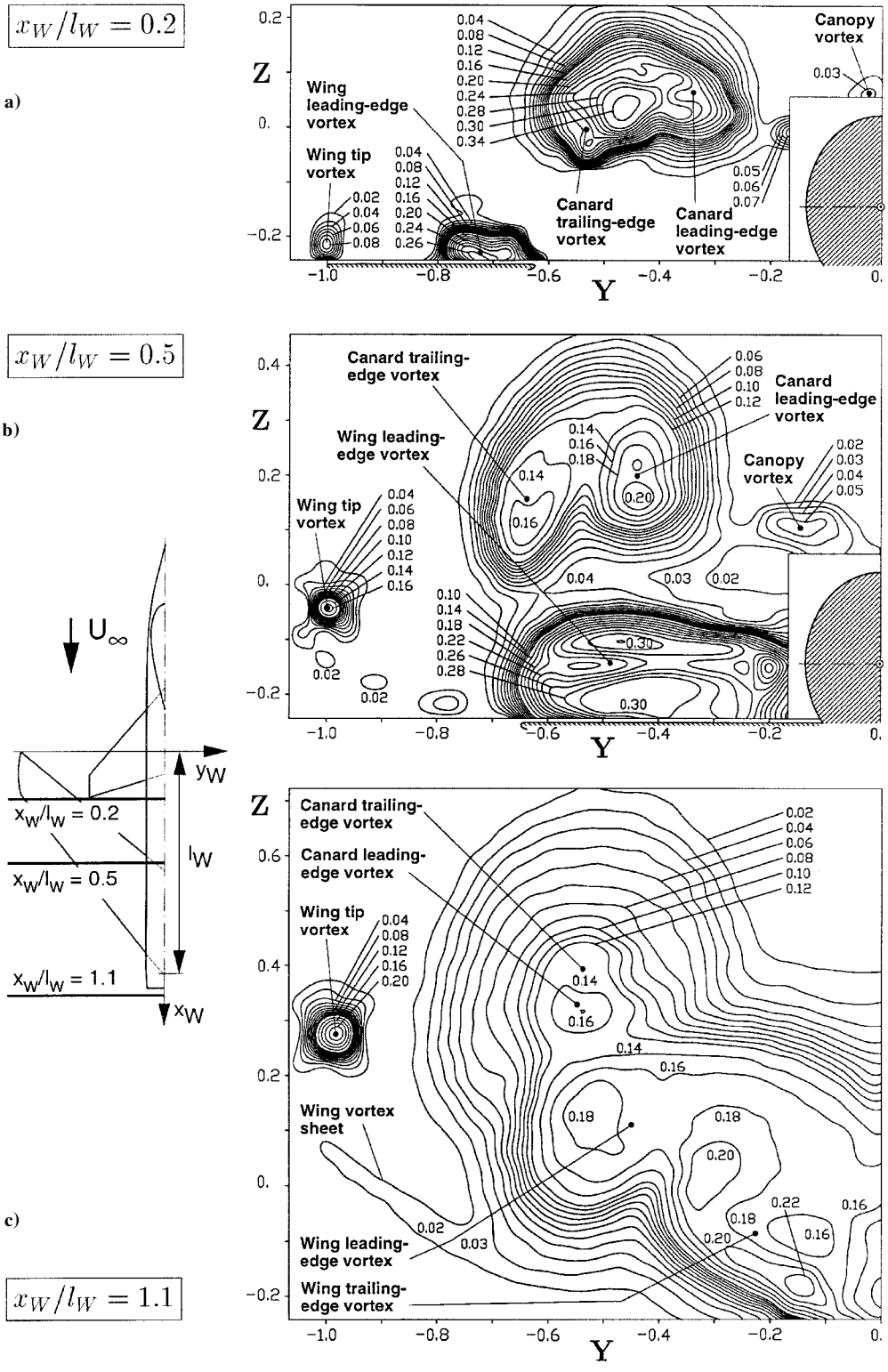

Fig. 15 Contours of axial rms velocity u_{rms}/U_∞ over the wing-body-canard configuration at $\alpha = 20$ deg and $Re_{l_\mu} = 0.46 \times 10^6$. Chordwise measurement stations x_W/l_W = a) 0.2, b) 0.5, and c) 1.1.

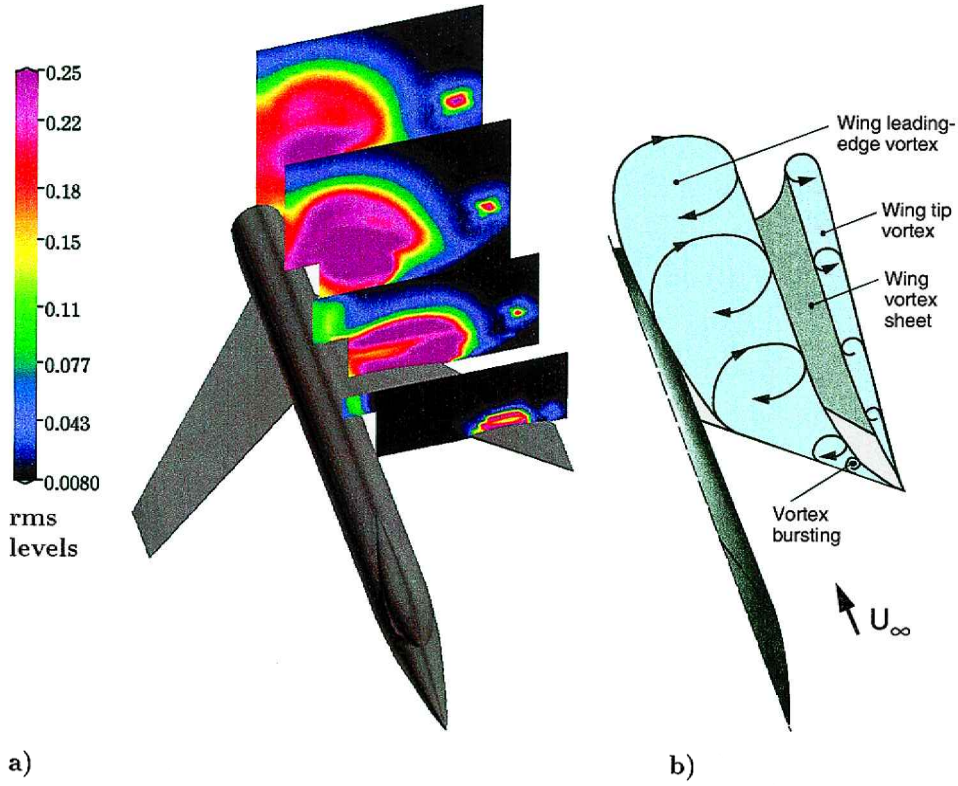

Fig. 16 Wing-body vortical flow characteristics at α = 30 deg and $Re_{l_\mu} = 0.46 \times 10^6$: a) Axial turbulence intensities u_{rms}/U_∞ at crossflow planes x_W/l_W = 0.2, 0.5, 0.8, and 1.1 and b) schematic representation.

Surveys of Turbulence Intensity

The turbulent flow structure is quantified by the rms values of the velocity fluctuations. They are typically nondimensionalized by the freestream velocity U_∞ to present the relative turbulence intensity in terms of percent of freestream. Here, only the axial rms component is considered (Figs. 14–17).

At $\alpha = 20$ deg and $x_W/l_W = 0.2$ the rms patterns of the wing-body configuration show two regions of high-velocity fluctuations (Fig. 14a). At $Y = -1.01$ the peak rms value of 10% indicates the center of the wing tip vortex. Its viscous core is defined by the steep gradients in the lateral and vertical velocity (Fig. 11a) resulting in an increased turbulence level. The peak rms value of 26% at $Y = -0.72$ denotes the center of the wing leading-edge vortex. The substantially higher turbulence intensity is caused by the bursting process where the adverse pressure gradient leads to a stagnation of the axial flow near the vortex axis (Fig. 9a). A local turbulence maximum above the fuselage indicates a vortex pair shed at the canopy. The leading-edge vortex is then considerably expanded at $x_W/l_W = 0.5$ covering the whole local span (Fig. 14b). Peak rms values reach levels of 34%. The pattern of the axial rms velocity associated with the burst leading-edge vortex is significantly changed. The maximum turbulence intensity is now concentrated on a limited radial range relative to the vortex axis. It was found that such rms patterns are typical for burst leading-edge vortices on slender delta wings.[20,25] The region of maximum turbulence intensity corresponds approximately to the points of inflection in the radial profiles of retarded axial velocity (Fig. 9b). Downstream of the wing trailing edge at $x_W/l_W = 1.1$, the leading-edge vortex starts to dissipate, documented by the further enlargement of the turbulent region and the decrease in rms values (Fig. 14c). The merging process of the neighbored port and starboard vortex sheets supports the disintegration of the primary vortex. A warp in the lower vortex sheet at $Y \approx -0.3$ marks the region between the outboard leading-edge vortex and the embedded inboard trailing-edge vortex.

For the canard-on configuration at $\alpha = 20$ deg and $x_W/l_W = 0.2$, the rms pattern for the wing tip and burst leading-edge vortex is very similar to that of the canard-off case (Fig. 15a). The canard leading- and trailing-edge vortices pass relatively high above the wing leading edge. Because of bursting, the canard vortex system is manifested by a large region of high-velocity fluctuations even higher than that for the burst wing primary vortex. At $x_W/l_W = 0.5$ the canard vortex system is characterized by two clearly separated rms maxima, with the inboard rms maximum representing the leading-edge vortex and the outboard rms maximum representing the trailing-edge vortex (Fig. 15b). Compared to the turbulence intensity of the upstream plane, the peak rms values are of lower magnitude. This, together with an increase in induced velocity (Figs. 10b and 12b), substantiates that restoring of the canard vortex system takes place over the wing. The canard interference itself leads to a reduction of the very high-velocity fluctuations existing close to the wing surface. Downstream, the wing and canard vortex systems are strongly connected by their shear layers. Throughout the merging process, the turbulence intensity associated with the wing and canard leading-edge vortices decreases (Fig. 15c). This develops more extensively for the wing leading-edge vortex than for the canard one. However, the wing tip vortex is kept relatively strong and stable indicated by the less expanded circular region of the rms pattern and an increase in the peak rms values.

The annular structure of maximum turbulence intensity, which is characteristic for the burst wing leading-edge vortex, is further documented for the wing-body configuration at $\alpha = 30$ deg (Fig. 16a). There, the described annular pattern of maximum rms values is already present at $x_W/l_W = 0.2$ with respect to the burst position, which is located close to the wing tip. A schematic flowfield representation highlights the downstream development of the vortex systems (Fig. 16b).

In addition to the rms patterns in streamwise direction, the distributions of axial velocity fluctuations are shown over the wing-body-canard configuration at $x_W/l_W = 0.8$ for various angles of attack, namely $\alpha = 10$, 20, and 30 deg (Fig. 17). With increasing α there is a tremendous enlargement of high turbulence intensity regions associated with the canard and wing vortex systems (Figs. 17a and 17b). It is seen that this process is mainly dominated by the burst wing and canard leading-edge vortices. Thus, at high α the merging of wing and canard vortices results in an area of highly fluctuating flow with a diameter of three times the fuselage height (Fig. 17c).

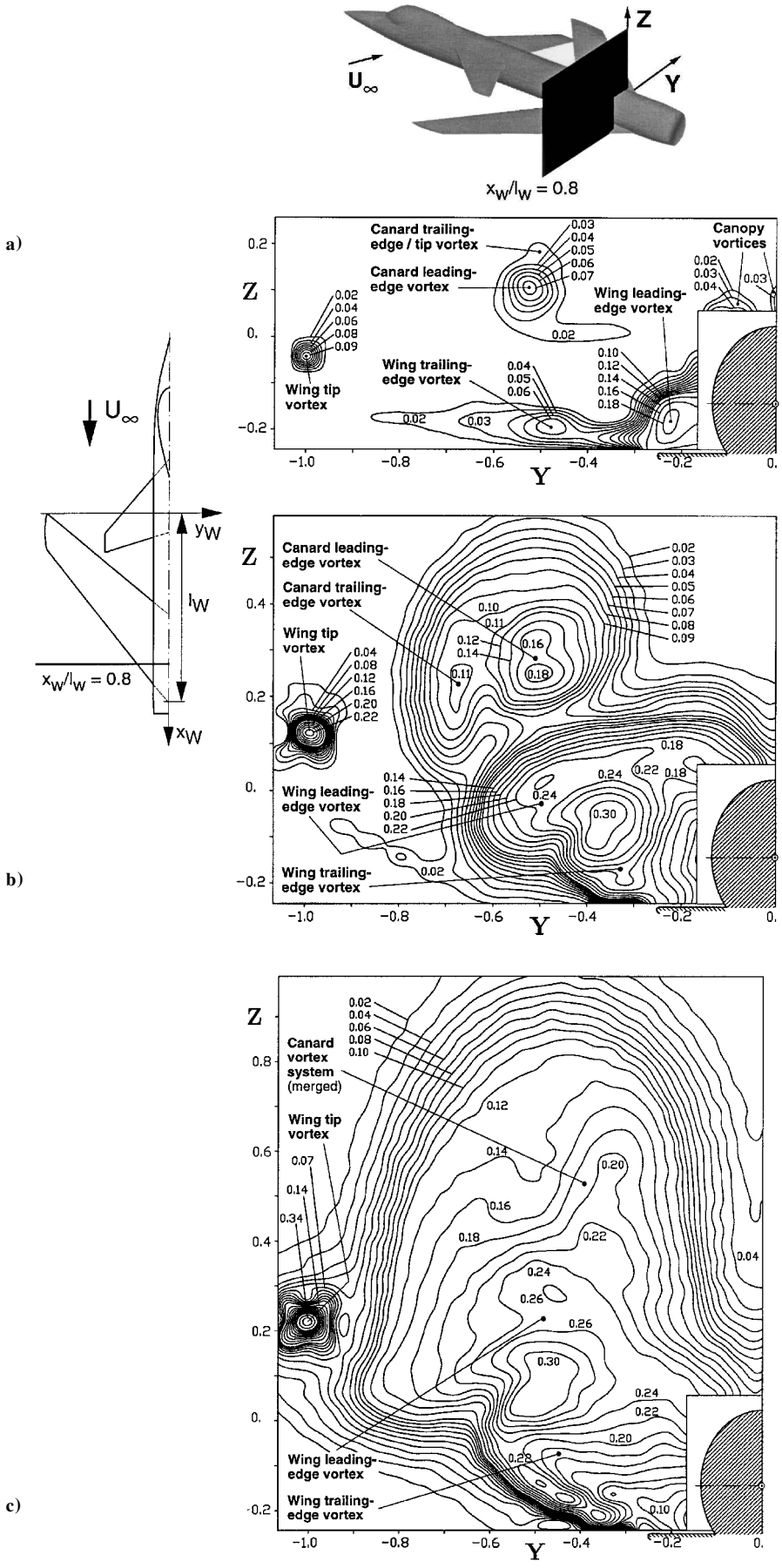

Fig. 17 Contours of axial rms velocity u_{rms}/U_∞ over the wing-body-canard configuration for the measurement station $x_W/l_W = 0.8$ at a) $\alpha = 10$, b) 20, and c) 30 deg and $Re_{l_\mu} = 0.46 \times 10^6$.

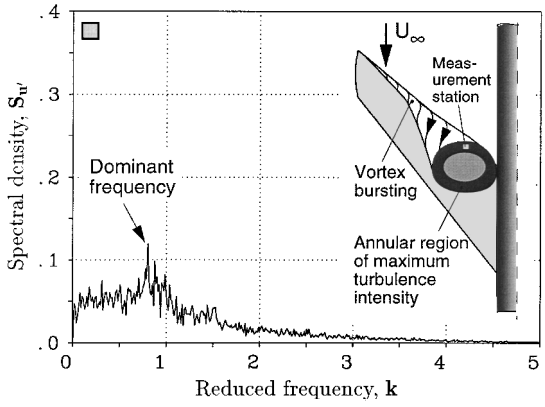

a) $\alpha = 20$ deg, $u_{rms}/U_\infty = 17.5\%$

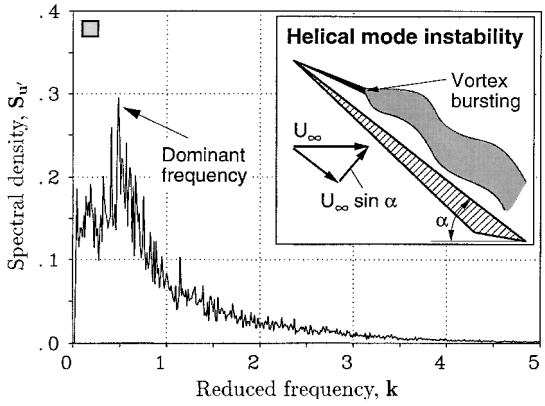

b) $\alpha = 30$ deg, $u_{rms}/U_\infty = 24.3\%$

Fig. 18 Power spectral densities of the axial velocity fluctuations $S_{u'}(k)$ measured at the burst wing leading-edge vortex at $x_W/l_W = 0.5$ and $Re_{l_\mu} = 0.46 \times 10^6$.

Therefore, single- or twin-finned configurations would be prone to buffeting.[25,26]

Spectral Content at High Angle of Attack

Spectral densities of the axial velocity fluctuations are evaluated at stations affected by the burst wing primary vortex, especially within the limited radial range of maximum turbulence intensity. There, the spectra exhibit pronounced narrowband peaks (Fig. 18). It shows that kinetic turbulent energy is channeled into a narrow band driven by quasiperiodic oscillations. This process is significant for the flow of burst leading-edge vortices, in particular, for the shear-layer region around the expanded vortex core.[20,25] It was found that the periodicity is linked to a helical mode instability with an azimuthal wave number of one.[20,27,28] Under these conditions breakdown is a leading mechanism for quasiperiodic loading on wing or fin(s).

Dominant Frequency

The dominant reduced frequencies according to the narrowband spectral peaks decrease with increasing angle of attack (Figs. 18a and 18b). This is because of the growth of the burst vortex core through which wavelengths of the quasiperiodic fluctuations increase while the related frequencies decrease. To compare the dominant reduced frequencies with the phenomena on delta-wing planforms, a frequency parameter based on the local semispan as a simplified length scale for the burst vortex core diameter and the sine of α is applied. For the FSW the dominant reduced frequencies are plotted together with literature data taken at delta-wing planforms of different sweep (Fig. 19).[20,27–29] The scaled reduced frequency values of the FSW and delta-wing planforms are in the same range [Eq. (1)]:

$$(f_{dom} x/U_\infty) \sin\alpha \cot\varphi_W \cong 0.28 \pm 0.06 \qquad (1)$$

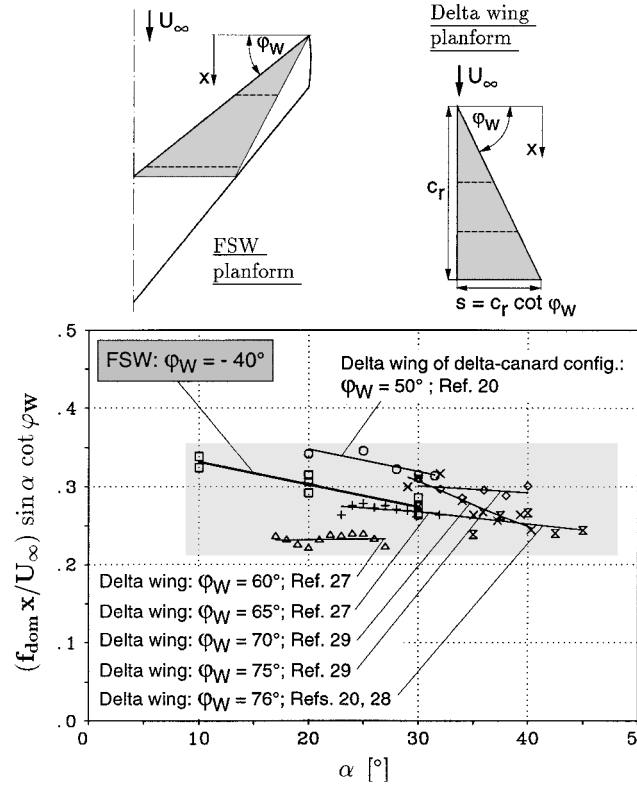

Fig. 19 Scaling of the reduced frequency of the dominant spectral peaks associated with the burst wing leading-edge vortex as a function of angle of attack. Comparison with literature data for delta-wing planforms.

Also, the reduced frequencies computed directly with the burst vortex core diameter match this range [Eq. (2)]:

$$(f_{dom} D_{core}/U_\infty) \cong 0.28 \pm 0.02 \qquad (2)$$

Conclusions

Extensive experimental investigations have been conducted on the low-speed flow environment of FSW configurations. Models employed include a wing-body and a wing-body-canard configuration with wing sweeps of −40 deg. Advanced hot-wire anemometry is used to measure the time-dependent flowfield velocities in cross-flow planes located at three different stations over the wing and at one station in the wake. The surveys were taken at angles of attack of 10, 20, and 30 deg at a test Reynolds number of 0.46×10^6. The main results of these investigations are as follows:

1) Complex vortex systems are shed on the wing-body and wing-body-canard configuration. For the canard-off case the wing tip vortex and the wing leading edge (primary) vortex with an opposite sense of rotation dominate the flowfield. At higher angles of attack, the wing primary vortex is accompanied by a weak secondary vortex. Moreover, the trailing-edge vortex sheet emanating from the inner wing part rolls up to form a trailing-edge vortex. In the wake the wing leading- and trailing-edge vortices merge, while the trailing-edge vortex is moved inboard and upward.

2) Bursting of the wing leading-edge vortex occurs already at moderate angles of attack in the outer wing region.

3) At the canard-on configuration the canard vortex system passes relatively high above the wing leading edge. It consists of the canard's leading-edge vortex combined with a trailing-edge vortex and the canard's tip vortex. Through wing influence this vortex system is moved upward and outboard. Over the wing the canard vortex system becomes reinforced, thus keeping its structure up to stations downstream of the wing trailing edge. At high α an intensive merging takes place between the burst wing and canard vortices.

4) The rms distributions indicate the increase in turbulence intensity toward the center of the wing tip vortex as well as an overall maximum of turbulence intensity for the burst wing and canard leading-edge vortices. Peak values reach levels of 34% of U_∞. Downstream of bursting the maximum turbulence intensity is concentrated within a characteristic annular region.

5) At stations near the trailing edge of the wing, the burst canard and wing leading-edge vortices are strongly expanded. This is associated with a large region of high turbulence intensity surrounding the midsection. Consequently, single- or twin-finned configurations may encounter severe buffet loads.

6) Distinct narrowband spectral peaks are found in the wake of the burst wing leading-edge vortex. They indicate quasiperiodic oscillations, which are proven to be typical for this flow type. For the dominant spectral peaks a reduced frequency parameter scaled with the sine of α and the local semispan gives values in the range of 0.28 ± 0.06.

References

[1]Herbst, W. B., "Future Fighter Technologies," *Journal of Aircraft*, Vol. 17, No. 8, 1980, pp. 561–566.

[2]Orlik-Rückemann, K. J., "Aerodynamic Aspects of Aircraft Dynamics at High Angles of Attack," *Journal of Aircraft*, Vol. 20, No. 9, 1983, pp. 737–752.

[3]Barlow, R. C., and Richey G. K., "Trends in Modern High Performance Aircraft," *Proceedings of the International Conference on Forward Swept Wing Aircraft*, Univ. of Bristol, Bristol, U.K., 1982, pp. 2.1–2.11.

[4]Zhang, B., and Laschka, B., "On Forward Swept-Wing's Aerodynamic Characteristics," *Journal of Northwestern Polytechnical Univ.*, Vol. 7, No. 3, 1989, pp. 321–328.

[5]du Boucheron, O., and Brocard, Y., "Comparison of Aerodynamic Characteristics of Aircraft Models with Forward and Aft Swept Wings at Mach Number 0.5," *Proceedings of the International Conference on Forward Swept Wing Aircraft*, Univ. of Bristol, Bristol, U.K., 1982, pp. I.6.1–I.6.11.

[6]Zhang, B., and Laschka, B., "On Aerodynamic Characteristics of Canard in Canard-Forward-Swept Wing Configuration," *Journal of Northwestern Polytechnical University*, Vol. 8, No. 3, 1990, pp. 327–334.

[7]Nangia, R. K., "Aspects of Forward Swept Wing Research at the University of Bristol," *Proceedings of the International Conference on Forward Swept Wing Aircraft*, Univ. of Bristol, Bristol, U.K., 1982, I.9.1–I.9.24.

[8]Löbert, G., "Spanwise Lift Distribution of Forward- and Aft-Swept Wings in Comparison to the Optimum Distribution Form," *Journal of Aircraft*, Vol. 18, No. 6, 1981, pp. 496–498.

[9]Schweiger, J., Schneider, G., Sensburg, O., and Löbert, G., "Design of a Forward Swept Wing Fighter Aircraft," *Proceedings of the International Conference on Forward Swept Wing Aircraft*, Univ. of Bristol, Bristol, U.K., 1982, pp. I.4.1–I.4.13.

[10]Nangia, R. K., and Shaw, D. E., "Theoretical Investigations into Forward Swept Wings," *Proceedings of the International Conference on Forward Swept Wing Aircraft*, Univ. of Bristol, Bristol, U.K., 1982, pp. I.10.1–I.10.8.

[11]Stanniland, D. R., "Aspects of the Aerodynamic Design of a Thin, Supercritical, Forward Swept Wing for a Combat Aircraft," *Proceedings of the International Conference on Forward Swept Wing Aircraft*, Univ. of Bristol, Bristol, U.K., 1982, pp. I.13.1–I.13.13.

[12]Weeks, T. M., and Leet, L. H., "The X-29A Forward Swept Wing Advanced Technology Demonstrator Program," *Proceedings of the International Conference on Forward Swept Wing Aircraft*, Univ. of Bristol, Bristol, U.K., 1982, pp. I.1.1–I.1.8.

[13]Saltzman, E. J., and Hicks, J. W., "In-Flight Lift-Drag Characteristics for a Forward-Swept-Wing Aircraft (and Comparisons with Contemporary Aircraft)," NASA-TP-3413, Dec. 1994.

[14]Griffin, K. E., "Measurement of Wake Interactions of a Canard and a Forward Swept Wing," U.S. Air Force Academy, USAFA-TN-82-4, Colorado Springs, CO, July 1982.

[15]Griffin, K. E., Haerter, E. C., and Smith, B. R., "Wake Characteristics and Interactions of the Canard/Wing Lifting Surface Configuration of the X-29 Forward Swept Wing Flight Demonstrator," U.S. Air Force Academy, USAFA-TN-83-7, Colorado Springs, CO, Aug. 1983.

[16]Griffin, K. E., and Jonas, F. M., "Wake Characteristics and Interactions of the Canard/Wing Lifting Surface Configuration of the X-29 Forward Swept Wing Flight Demonstrator," AIAA Paper 83-1835, July 1983.

[17]Breitsamter, C., "Vortex-Dominated Flowfields at Forward Swept Wing Configurations," *Proceedings of the German Aerospace Congress of the German Aerospace Society*, Vol. I, Deutsche Gesellschaft für Luft-und Raumfahrt-Lilienthal-Oberth e.V. (DGLR), München, 1997, pp. 517–526.

[18]Bendat, J. S., and Piersol, A. G., *Random Data: Analysis and Measurement Procedures*, Wiley, New York, 1971, pp. 170–193.

[19]Breitsamter, C., and Laschka, B., "Velocity Measurements with Hot-Wires in a Vortex-Dominated Flowfield," *Wall Interference, Support Interference and Flow Field Measurements*, Brussels, Belgium, 1993, pp. 11-1–11-13 (AGARD-CP-535).

[20]Breitsamter, C., "Turbulente Strömungsstrukturen an Flugzeugkonfigurationen mit Vorderkantenwirbeln," Ph.D. Dissertation, DM 18432, Technische Univ. München and Herbert Utz Verlag Wissenschaft (Aerodynamik), Germany, (ISBN 3-89675-201-4) June 1997.

[21]Payne, F. M., "The Structure of Leading Edge Vortex Flows Including Vortex Breakdown," Ph.D. Dissertation, Dept. of Aerospace and Mechanical Engineering, Univ. of Notre Dame, IN, May 1987.

[22]Payne, F. M., Ng, T. T., and Nelson, R. C., "Seven Hole Probe Measurement of Leading Edge Vortex Flows," *Experiments in Fluids*, Vol. 7, No. 1, 1989, pp. 1–8.

[23]Rohne, W., "Experimentelle Untersuchung des Strömungsfeldes und der aerodynamischen Größen an einer vorwärtsgepfeilten Flugzeugkonfiguration," M.S. thesis, Lehrstuhl für Fluidmechanik, TR FLM-95/32, Technische Universität München, Germany, June 1995.

[24]Tobak, M., and Peak, D. J., "Topology of Threedimensional Separated Flows," *Annual Review Fluid Mechanics*, Vol. 14, 1982, pp. 61–85.

[25]Breitsamter, C., and Laschka, B., "Turbulent Flow Structure Associated with Vortex-Induced Fin Buffeting," *Journal of Aircraft*, Vol. 31, No. 4, 1994, pp. 773–781.

[26]Canbazoglu, S., Lin, J.-C., Wolfe, S., and Rockwell, D., "Buffeting of a Fin: Streamwise Evolution of Flow Structure," *Journal of Aircraft*, Vol. 33, No. 1, 1995, pp. 185–190.

[27]Gursul, I., "Unsteady Flow Phenomena over Delta Wings at High Angle of Attack," *Journal of Aircraft*, Vol. 32, No. 2, 1994, pp. 225–231.

[28]Breitsamter, C., "Experimental Studies of the Turbulent Flow Structure of Leading-Edge Vortices," *Notes on Numerical Fluid Mechanics* (NNFM), New Results in Numerical and Experimental Fluid Mechanics, Vol. 60, Vieweg, 1997, pp. 79–86.

[29]Mabey, D. G., "Unsteady Vortex Flow Phenomena on Delta Wings at High Angles of Incidence," *Proceedings of the 20th Congress of the International Council of the Aeronautical Sciences*, Vol. 1, American Institute of Aeronautics and Astronautics, Inc., Reston, VA, 1996, pp. 1167–1176 (ICAS Paper 96–1.6.1).

Color reproductions courtesy of Institute for Fluid Mechanics of the Technische Universität München.